Demonstration of Large Mode-Hop-Free Tuning in Narrow-Linewidth Heterogeneous Integrated Laser

Paolo Pintus, *Senior Member, IEEE*, Joel Guo, Minh A. Tran, Warren Jin, Joe Liang, Jonathan Peters, Chao Xiang, Osgar John Ohanian III, and John E. Bowers, *Life Fellow, IEEE*

***Abstract*—Continuously tunable lasers with a narrow linewidth are at the core of a large number coherent optical systems. Integration of these devices on a single chip will enable a large number of applications that require minimal size, weight, power, and cost. In this work, we demonstrate a 3 nm-continuously tunable laser operating around 1550 nm with a narrow intrinsic linewidth of 5.7 kHz. The device is fully integrated on a silicon-on-insulator platform and the optical gain is provided by a bonded III-V layer. The narrow laser linewidth is attained with an extended cavity that consists of a Vernier ring-based mirror and a passive waveguide. To reach the record continuous (mode-hop-free) tuning range of 3 nm (375 GHz), we demonstrate a method for synchronously tuning the Vernier resonances together with the cavity longitudinal modes, both thermally controlled. In the current laser, the mode-hop-free tuning range is limited by the maximum heating power, but it can be extended over more than 10 nm (1.25 THz) by optimizing the integrated heater design.**

***Index Terms*—Integrated optoelectronics, laser tuning, semiconductor lasers, silicon photonics.**

I. Introduction

NARROW-LINEWIDTH lasers with a large continuous tuning range play a fundamental role in high-resolution coherent optical sensing and spectroscopy. Such lasers are instrumental for optical coherence tomography (OCT) [1], [2], optical frequency domain reflectometry (OFDR) [3], [4], light detection and ranging (LiDAR) [5], [6], [7], and atomic physics [8], [9]. In all of these applications, narrow linewidth laser allows high precision measurements, while continuous mode-hop-free wavelength tuning ensures that no frequencies are neglected and the optical spectrum is acquired without discontinuities. Integration of mode-hop-free tunable lasers is highly desirable due to the unparalleled reduction in size, weight, power, and cost (SWaP-C). For instance, these kinds of lasers can enable OFDR in photonic integrated circuits for high-resolution monitoring of strain and temperature in aerospace structures [10], [11]. Similarly, lightweight and low-cost continuously tunable lasers are essential in LiDAR systems for self-driving cars, robots, and drones [7], [12]. Despite the tremendous progress in integrated photonics and the large industrial interest, simultaneous narrow linewidth and wide mode-hop-free tunability in on-chip lasers has not been demonstrated yet.

Narrow-linewidth continuously tunable lasers require a resonant cavity with a large quality factor to achieve high-coherence [13], [14], while changing the optical cavity length through varying the refractive index or the cavity size shifts the laser wavelength [15]. Generally, light in a cavity can resonate at multiple frequencies (longitudinal modes), and a single frequency (single mode) can be selected by engineering either the optical gain spectrum, the cavity length, the mirror reflectivity, or intracavity elements such as a grating or etalon. Even if a laser achieves single mode operation at a specific wavelength; during tuning, one (or more) additional longitudinal modes can begin lasing and compete with each other. In some cases, the initial mode stops lasing, leading to a jump of the laser wavelength, referred to as *mode hopping*. This phenomenon is detrimental for all the applications that require a continuous wavelength scan.

The external-cavity diode laser (ECDL) is the most effective laser configuration to obtain both narrow laser linewidth and wide wavelength tuning range. Narrow linewidth can be achieved using a low-loss passive section that extends beyond the active part of the laser cavity [14], [16]. A tunable element within the cavity (a filter or a mirror) guarantees single-mode behavior [15], [17]. Single-mode tunable lasers with a narrow linewidth ($<$10 kHz) have been recently demonstrated on several integrated platforms [18], [19], [20], [21], [22]; however, the largest mode-hop-free tuning is so far 0.22 nm (28 GHz) [19], [23].

Two kinds of tunable mirrors are normally employed to continuous tune the laser while maintaining a narrow linewidth: ring

Manuscript received 13 February 2023; revised 15 June 2023 and 3 July 2023; accepted 7 July 2023. Date of publication 11 July 2023; date of current version 2 November 2023. This work was supported in part by NASA under Grant 80NSSC19C0015, in part by U.S. Air Force under Grant FA9300-19-C-2002, and in part by DARPA MTO LUMOS Program under Grant 442650-59747. *(Corresponding author: Paolo Pintus.)*

This work did not involve human subjects or animals in its research.

Paolo Pintus is with the Department of Electrical and Computer Engineering, University of California, Santa Barbara, Santa Barbara, CA 93106 USA, and also with the Department of Physics, University of Cagliari, 09042 Monserrato, Italy (e-mail: ppintus@ece.ucsb.edu).

Joel Guo, Jonathan Peters, Chao Xiang, and John E. Bowers are with the Department of Electrical and Computer Engineering, University of California, Santa Barbara, Santa Barbara, CA 93106 USA (e-mail: joelguo@ucsb.edu; peters@ece.ucsb.edu; cxiang@ece.ucsb.edu; bowers@ece.ucsb.edu).

Minh A. Tran is with the Department of Electrical and Computer Engineering, University of California, Santa Barbara, Santa Barbara, CA 93106 USA, and also with the Nexus Photonics, Goleta, CA 93117 USA (e-mail: minhtrananh@gmail.com).

Warren Jin is with the Department of Electrical and Computer Engineering, University of California, Santa Barbara, Santa Barbara, CA 93106 USA, and also with the Anello Photonics, Santa Clara, CA 95054 USA (e-mail: warren@ece.ucsb.edu).

Joe Liang and Osgar John Ohanian III are with the Luna Innovations Incorporated, Blacksburg, VA 24060 USA (e-mail: hongliang.joe.liang@gmail.com; ohanianj@lunainc.com).

Color versions of one or more figures in this article are available at https://doi.org/10.1109/JLT.2023.3294235.

Digital Object Identifier 10.1109/JLT.2023.3294235

resonators [18], [19], [20], [21], [23], [24] and grating reflectors [25], [26], [27], [28], [29]. With equal intrinsic linewidth, ring mirrors exhibit a more compact footprint, with a radius of a few tens of micrometers [19], while equivalent gratings can be more than a centimeter long [27]. In addition, for lasers designed to operate at the telecom wavelengths, grating mirrors usually require high-resolution electron beam lithography, while ring resonators can be fabricated using standard lithography processes, making them more cost effective for massive production.

Another challenge of tunable lasers is performing a wide wavelength scan. A method that has been widely explored consists of moving mirrors [30], [31], [32], [33], [34]. However, many sensing applications require lasers to be resistant to vibration and shock, significantly complicating this approach and favoring solid-state devices. More viable solutions employ electrically tunable elements in the laser cavity, which are used to change the optical length of the recirculating light. Integrated elements can be tuned via thermo-optic [19], [20], [21], [23] and electro-optic [24], [35], [36] effects. Choosing the most efficient tuning effect depends on the material system and the laser configuration. Adjusting the wavelength of a distributed feedback (DFB) laser is typically done by controlling the current in the active section [28]. However, this can result in non-constant output power over the tuning range. Similarly, a current can be used in a distributed Bragg reflector (DBR) laser to control the reflectivity of the gratings through the carrier injection [26], but this can decrease the output power and widen the laser linewidth due to free carrier absorption [37]. An alternative method is to change the temperature of the DFB laser cavity [38] or just the gratings in the DBR laser [39], [40], [41]. However, this approach may require a significant amount of power when the mirrors are significantly extended, as in the case of narrow laser linewidths. In contrast, the wavelength of a ring-based laser can be tune controlling the temperature of ring resonators and integrated phase shifters with minimal power consumption and without affecting the laser linewidth [19]. Moreover, controlling the tuning elements independently of the active section results in a constant output power across the tuning range wavelengths. Although integrated phase control elements are ideal for robust tuning in an integrated device, specific algorithms still need to be developed to avoid mode hops between longitudinal lasing modes [23], [26].

In this work, we demonstrate an integrated heterogeneous laser in silicon photonics with a 5.7 kHz intrinsic linewidth that can be continuously tuned in the third telecom window ($\sim$1550 nm). The optical gain section is implemented by bonding a III-V multi-quantum well (MQW) epitaxial layer onto a silicon waveguide, and narrow fundamental linewidth lasing is achieved using a resonantly enhanced extended cavity. The lasing wavelength is controlled using two thermally-tunable elements: a Vernier multi-ring-based mirror and a phase shifter. Both the mirror and the phase shifter benefit from the large thermo-optic coefficient of silicon. To avoid a mode hopping, a control algorithm is developed to simultaneously tune the Vernier mirror and the phase shifter, achieving a single-mode mode-hop-free tuning range of 3 nm (375 GHz). The tuning range is currently limited by the phase shifter, but it can be extended to more than 10 nm (1.25 THz) by increasing the heater efficiencies with lateral air trenches and depositing a thinner silica cladding [42], [43].

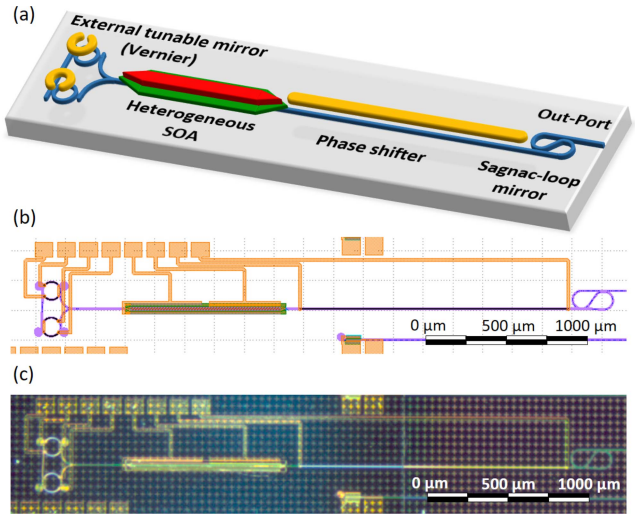

Fig. 1. Integrated mode-hop-free tunable heterogeneous laser. Not-to-scale schematic view of the device (a), mask layout of the laser (b), and fabricated device (c).

II. Device Layout

The heterogeneously integrated tunable laser under investigation is shown in Fig. 1. A schematic view of the device, not to scale, is shown in Fig. 1(a), whereas Fig. 1(b) and (c) show the mask layout and a microscope image of this laser, respectively.

The passive silicon waveguides and mirrors are defined by etching 231 nm trenches into a 500 nm silicon-on-insulator (SOI) layer with 1 μm buried oxide (BOX). High precision control of the etch depth during the fabrication of the waveguides is achieved using an in-situ etch depth monitor system (Intellemetrics LEP500) [44]. The choice to use a 1 μm-thick BOX substrate is motivated by the need to enhance heat dissipation of the laser, thereby preventing performance degradation at high temperature [45], [46].

The output mirror is formed by a Sagnac-loop and has a reflectivity of 50%, determined by the coupling strength of the directional coupler. On the other end of the laser cavity, a tunable reflector is implemented with a Vernier ring-based mirror (external tunable mirror). The ring radii of the two rings are 60 μm and 62.5 μm. With a free-spectral-range (FSR) of 1.73 nm and 1.66 nm, respectively, they provide a Vernier FSR of 41.5 nm. This reflector serves two purposes: it acts as a single wavelength filter and it enhances the laser cavity length to provide a narrow fundamental linewidth. To perform a side-mode suppression ratio of Vernier filter $>$15 dB and fundamental linewidth $<$10 kHz, the power coupling coefficient between the rings and the waveguide is set to $\kappa^2 = 12.5\%$ [14], [19]. The lasing mode of the cavity is controlled via thermo-optic tuning of both a 1.575 mm-long passive section (i.e., phase shifter) and the Vernier mirror.

The 1 mm-long bonded III-V section acts as a heterogeneously semiconductor optical amplifier (SOA). Three InAlGaAs quantum wells provide the optical gain in the laser cavity [47]. The silicon width in the amplifier is chosen to be 850 nm, which balances out the low internal loss and the high gain required for the laser.

The light is coupled from the chip using a tapered waveguide edge coupler [48]. This solution is preferred over grating couplers because it offers a larger transmission bandwidth and lower reflection over a wider range of wavelengths [49]. In order to match the optical mode of the waveguide with the one of the fiber, the width of a rib waveguide is tapered from 800 nm to 4 μm at the edge of the chip (i.e., *direct taper*). At the chip edge, the mode mismatch between the waveguide mode and the fiber mode limits the power coupling to -7.5 ± 0.6 dB/facet. Although the direct tapered waveguide is less efficient when compared to an inverse tapered one [48], [49], this strategy is optimal when the BOX layer is thin, because the mode is mainly confined in the waveguide and does not leak into the silicon substrate. A potential solution to enhance the fiber-to-chip coupling in the presence of a 1 μm BOX layer is to incorporate an inverse taper and perform silicon substrate etching at the edge of the chip [50]. This approach effectively prevents mode leakage into the substrate, resulting in the creation of a suspended silica waveguide for coupling light into the fiber and reducing the coupling loss below 2 dB/facet.

The laser wavelength shifts linearly by increasing the temperature of the two rings and the phase shifter via the thermo-optic effect. A continuous current in each metal heater is used to locally control the temperature of the corresponding device sections underneath, see Fig. 1. The relation among the wavelength shift, $\Delta\lambda$, the temperature variation, ΔT, the dissipated power, P, and the electrical current in the heater, I, is

$$\Delta\lambda \sim \Delta T \sim P \sim I^2 \tag{1}$$

as outlined in [42]. To clarify, the proportional constant between P and I^2 is the resistance of the heater, R.

The key to achieving continuous laser tuning is determining the wavelength tuning rates of the three heaters with current. Knowing this, the response of Vernier mirror can be tuned in unison with the longitudinal modes of the cavity to prevent mode hoping.

III. Laser Characterization

We characterize the output power and wavelength tuning of the laser with the device on a thermally controlled stage at a temperature of 20 °C. The output light of the laser is equally split between a power meter (Agilent 81634B) and a wavelength meter (Yokogawa AQ6150).

The light-current curve shown in Fig. 2 is measured by ramping up the current in the active section while all heaters (rings and phase section) are off. At a gain current of 200 mA, we measure an output power of 3 mW with a voltage of 2 V, resulting in a wall-plug efficiency (WPE) of approximately 0.75%. By reducing propagation loss, optimizing the laser epitaxial structure, and implementing better heat dissipation, a significantly higher WPE

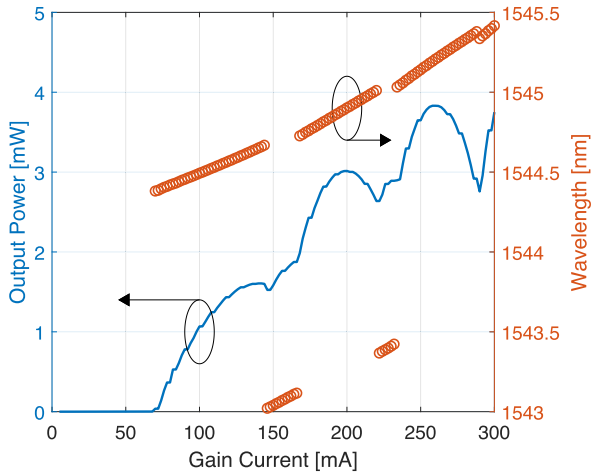

Fig. 2. On-chip output power of the laser (left-axis) and lasing wavelength (right-axis) as a function of the gain current. The laser output power is estimated based on the power measured at the power meter (Agilent 81634B),considering the system loss (4.0 ± 0.1 dB, mainly due to 1×2 beam splitter and isolator insertion loss) as well as the edge coupler loss (7.5 ± 0.6 dB/facet). The heater of the ring resonators and the phase shifter are off.

can be reached. Indeed, similar lasers to the one discussed in this study have demonstrated efficiencies greater than 12% [51]. It is worth noting that while the estimated WPE may appear relatively low, achieving mode-hop-free tuning is independent of improving the WPE. For the same range of current used to measure the light-current curve, the lasing wavelength hops in the range between 1543.0 nm and 1545.5 nm because the effective optical length of the laser cavity changes due to thermal heating and carrier injection in the active section.

After setting the gain current, the two rings are thermally tuned to a desired wavelength of 1542 nm in a coarse manner, while the heater of the phase shifter is kept off. The ring heaters are then finely tuned to maximize the output power [14]. At a gain current of 270.3 mA and ring currents of $I_{R1} = 7.91$ mA and $I_{R2} = 3.37$ mA, we measured the frequency noise spectrum of the laser, as shown in Fig. 3. Frequency noise measurements were taken with a commercial OEwaves OE4000 optical phase noise analyzer utilizing a quadrature-biased unbalanced Mach-Zehnder interferometer-based frequency discriminator [14]. At low offset frequencies, technical noise dominates (from the environment or potentially current source). However, the majority of these noises decrease significantly at the higher frequency range, where we can observe the laser quantum noise. This white frequency noise floor is used to compute a corresponding Schawlow-Townes (fundamental) linewidth of 5.7 ± 0.6 kHz. While it is possible to measure a narrower laser linewidth under detuned loading conditions [14], it is generally easier to control the laser when the output power is at its maximum.

In the device under test, the laser linewidth is primarily limited by the quality factor of the rings, which is approximately $Q \simeq 25$ K. A narrower linewidth can be achieved by designing smaller coupling coefficient κ [14]. In the specific platform under consideration (500 nm-thick SOI with 231 nm-deep trenches), the minimum demonstrated propagation loss is

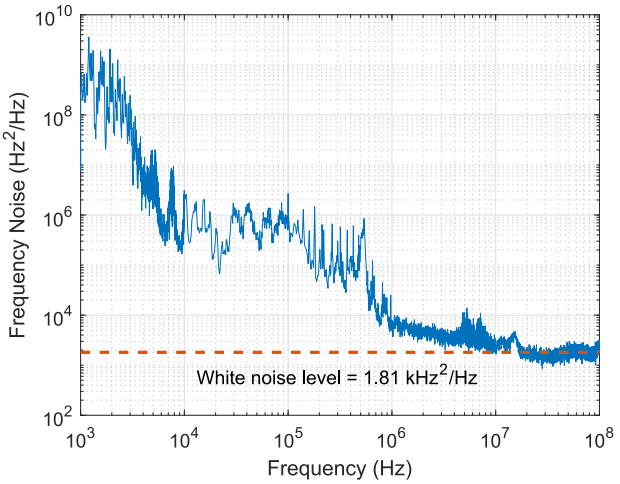

Fig. 3. Frequency noise spectrum measured at the laser wavelength of 1542 nm. The current in the gain section is set at 270.3 mA and the current in the two rings are 7.91 mA and 3.37 mA. The heater of the phase shifter is kept off. From the white frequency noise floor, we extracted a Schawlow-Townes (fundamental) linewidth of 5.7 ± 0.6 kHz.

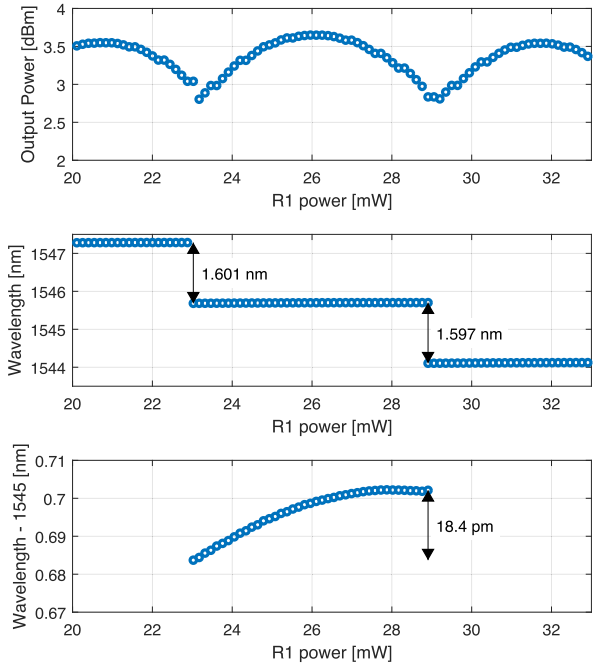

Fig. 4. Output power (top), mode hopping (central), and mode-hop-free range (bottom) of the laser when a single ring of the Vernier mirror is tuned. In the central plot, two jumps in the laser wavelength are highlighted (mode hops). The bottom panel is a zoom of the central one. There, we show the average continuous tuning range when a single ring is controlled.

approximately 1 dB/cm [52], resulting in an intrinsic quality factor $Q_0 \simeq 650$ K. For $\kappa^2 < 0.01$, the quality factor Q reaches the value of Q_0, corresponding to the narrowest achievable linewidth of 200 Hz [14].

We have previously reported similar fundamental linewidths in dual-ring devices across over 40 nm tuning in both the C-band [19] and O-Band [20]. However, this tuning range was not previously demonstrated with continuous tuning. A look up table—the set of current values for a specific emission wavelength —would be necessary for such a wide range and the same longitudinal mode would not be preserved. In the following sections, we present a method for continuous mode-hop-free tuning, which preserves the same mode.

IV. Mode Hop Analysis

Synchronous control of all the tunable elements is critical for performing mode-hop-free continuous tuning of the laser. In order to develop an effective algorithm, we first analyzed the laser behavior when each element is independently controlled.

First, we analyze the behavior of the laser when the power in one of the ring heaters increases. As shown in Fig. 4, the mode hop is about 1.6 nm, which matches the FSR of a single ring. The mode-hop-free tuning range, however, is limited to approximately 18 pm. A similar behavior is observed when the other ring is thermally tuned.

It is worth noting the behavior of the laser wavelength: it increases linearly immediately after a mode-hop; saturates when the laser power reaches its maximum; and slightly blue shifts before the next mode hop. This nonlinear behavior suggests that two competitive effects might be present in the ring resonator: the red-shift of the thermo-optic effect and the blue-shift of the free carrier injection [53]. Free carriers are produced in silicon due to two-photon absorption, which is caused by the high optical power in the ring resonator. Indeed, if the optical

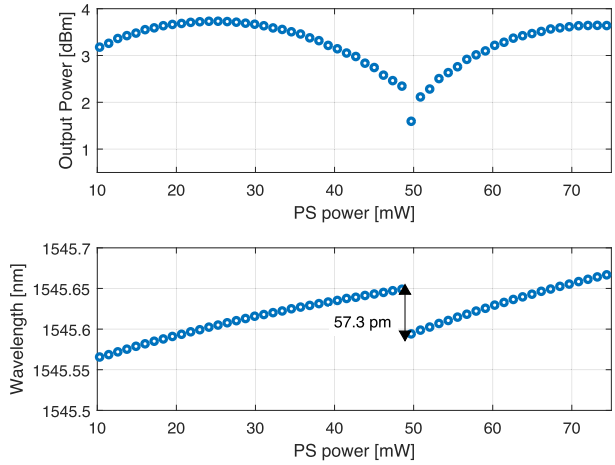

Fig. 5. Output power (top) and wavelength (bottom) of the laser when the phase shifter is tuned. A mode hop is present in the middle of the current sweep.

power in the laser cavity is tens of milliwatts, the optical power in the ring resonator is nearly ten times this value (i.e., the build-up factor for an add-drop ring is $1/\kappa^2$ [54]).

By thermally controlling the phase shifter, the mode-hop-free tuning range extends over 100 pm with a mode hop of 57.3 pm, as shown in Fig. 5. In this case, the mode hop matches the spectral distance between two longitudinal modes. With this information, we can revisit the result shown in Fig. 2. There, a large mode hop (e.g., $\Delta\lambda \simeq 1.6$ nm at I$\simeq$150 mA) corresponds to the FSR of the

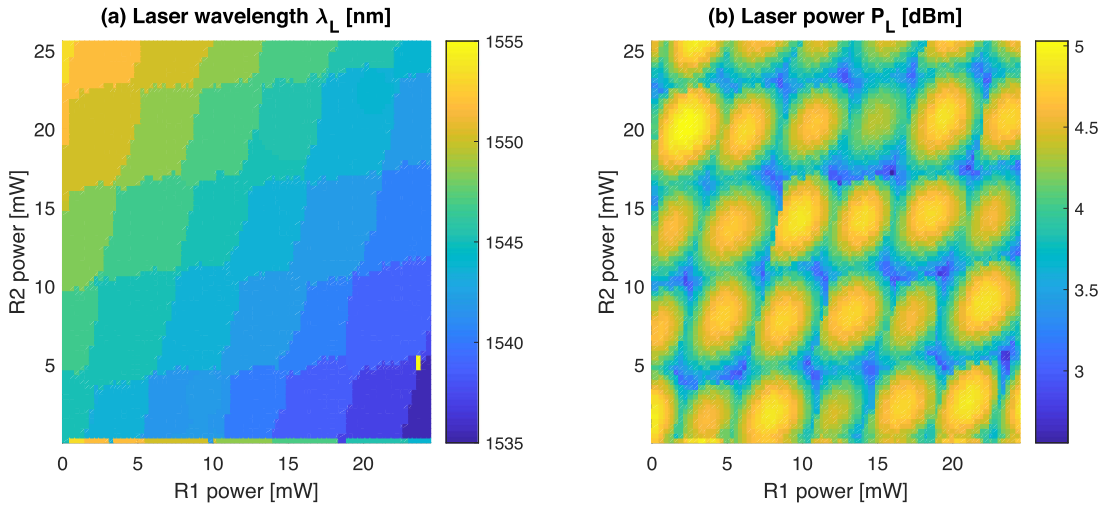

Fig. 6. 2D tuning map of the (a) laser wavelength, λ_L, and (b) output power, P_L, when the two rings are thermally controlled.

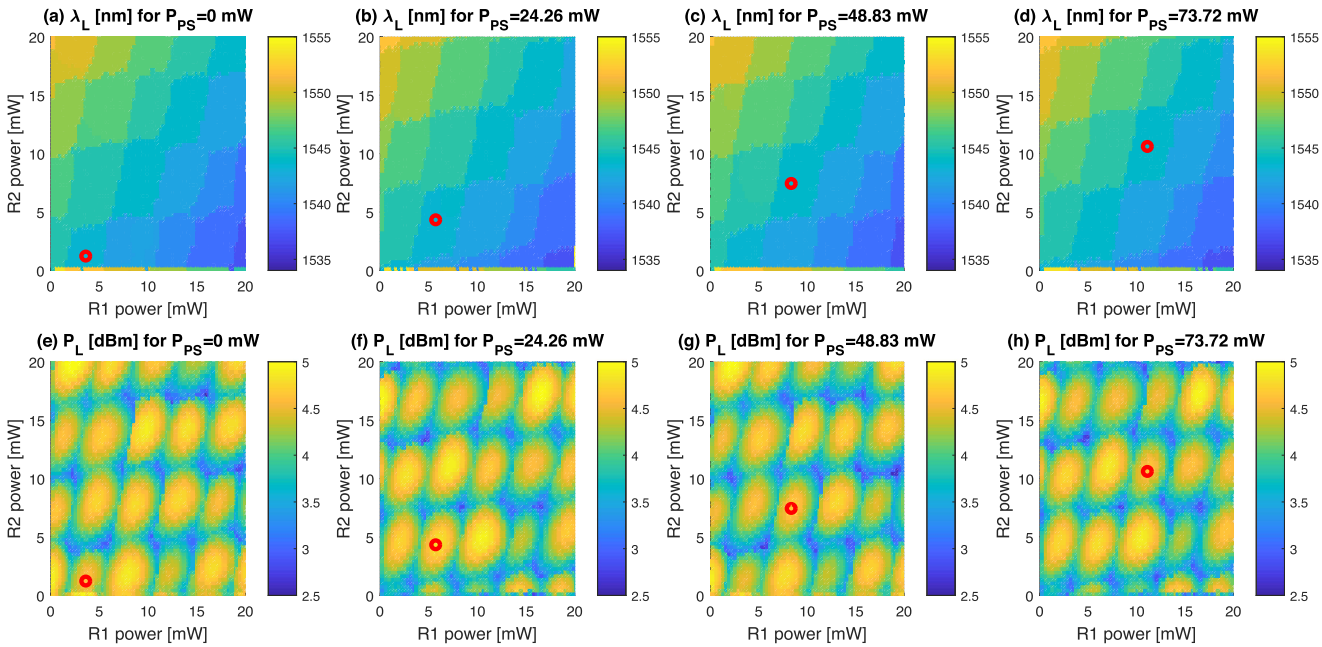

Fig. 7. 2D tuning map of the laser wavelength, λ_L, and output power, P_L, when the two rings are thermally controlled, for different power of the phase shifter: 0 mW, 24.26 mW, 48.83 mW, and 73.72 mW.

Vernier mirror, while a small mode hop is due to longitudinal modes in the cavity (e.g., $\Delta\lambda \simeq 60$ pm at I$\simeq$290 mA).

We extend our analysis by independently tuning both rings of the Vernier mirror, without applying power to the phase shifter. A 2D tuning map for both the laser wavelength and the output power is shown in Fig. 6. We observed a staircase behavior in the measured wavelength, corresponding to Vernier ring modes of the ring resonators acting as a filter ($\simeq$1.6 nm jump in color contour of Fig. 6(a)). Within these Vernier ring modes there are diamond shaped plateaus. In each plateau, the wavelength continuously spans over 20 pm. As the power of the ring heaters increases along the main diagonal of the plot (from bottom left to top right) the laser wavelength shows a minor mode hop ($\simeq$60 pm) between two consecutive diamond plateaus. This corresponds to two consecutive longitudinal cavity modes. Comparing the results in Fig. 6(a) with the output laser power reported in Fig. 6(b), we observe that the output laser power has a local maximum at the center of each diamond region, where the wavelength is roughly constant. The mode hops occur at the edge of each diamond areas, where the power drops.

To complete our investigation, we measure the 2D tuning maps for different phase shifter (PS) power, as shown in Fig. 7. Comparing the different maps, we observe that the pattern of

wavelength and output power is preserved and shifts northeast when the heat in the phase section increases.

To achieve continuous tuning, the key is to follow the path of the local maximum of the optical output power. This approach has recently been demonstrated to be successful in a hybrid integrated indium phosphide diode laser with silicon nitride phase shifter and ring-based mirror [23]. In this seminal work, the authors were able to achieve 0.22 nm mode-hop-free tuning using a theoretical model that guides the tuning of each ring with respect to the phase section. In our work, developing an accurate theoretical model to control the heaters is more challenging due to several factors. The high thermo-optic coefficient of silicon allows us to achieve a larger continuous tuning range, but also leads to greater thermal cross-talk. The smaller footprint of the heterogeneous silicon photonic laser is another factor contributing to the larger thermal cross-talk, as it results in the devices being positioned closer to each other. Additionally, the ring resonance does not change linearly with temperature, but rather exhibits nonlinear behavior when tuning the silicon rings, as shown in Fig. 4. It is important to note that in order to avoid mode hop, the resonance of the rings in the Vernier mirror must be controlled with a precision of ± 9 pm across the entire tuning range (see Fig. 4). To determine the relationships for simultaneous tuning of the ring resonators with the phase section, we developed a numerical method, which is presented in the following section.

V. Mode-Hop-Free Tuning Algorithm

Since mode hops are accompanied by power drops, we can achieve mode-hop-free tuning by tracking a local maximum of the output power. This approach also ensures that we are operating near optimal linewidth, as the longitudinal cavity modes and Vernier modes are aligned and the linewidth is inversely proportional to the output power. It is important to note that simply maximizing output power does not result in the narrowest linewidth. In fact, detuned loading to the red side of the resonance can initiate an optical negative feedback loop that further stabilizes the laser frequency [14]. However, operating at the highest output power can still yield a fundamental linewidth of the order of kHz and simplifies the control of the laser.

The tuning maps shown in Fig. 7 are central to extracting the relations between a laser wavelength and the current injected in the heaters of the rings (I_{R1} and I_{R2}), and the phase shifter (I_{PS}). In Algorithm 1, we report the procedure developed to collect the data shown in the tuning map. In line 3–5 of the algorithm, the currents are chosen such that the heater power varies linearly, see (1). This produces a tuning map with uniformly distributed output power maxima, as shown in Figs. 6(b) and 7(e)–(h).

For an increased heater power in the PS, tracking the maximum laser power requires higher heater power in the two rings. Starting from this consideration, we develop Algorithm 2: first, we consider the tuning map of the output power when the power (so the current) of the PS heater is set and select a local maximum. Then, we consider the tuning map measured with a larger power in the PS, and we calculate the cross-correlation between those tuning maps. The indices of

Algorithm 1: Mode-Hop-Free Algorithm — Data Acquisition.

1: $i_{R1,M}, i_{R2,M}, i_{PS,M} \leftarrow$ Set the maximum of the heater currents
2: N, M, $P \leftarrow$ Set the number of points for the heater sweeps
3: $i^2_{R1} = linspace(0, i^2_{R1,M}, N)$
4: $i^2_{R2} = linspace(0, i^2_{R2,M}, M)$
5: $i^2_{PS} = linspace(0, i^2_{PS,M}, P)$
6: **for** $p = 1 : P$ **do**
7: set phase shifter current $\leftarrow i_{PS}[p]$
8: **for** $n = 1 : N$ **do**
9: set ring 1 current $\leftarrow i_{R1}[n]$
10: **for** $m = 1 : M$ **do**
11: set ring 2 current $\leftarrow i_{R2}[m]$
12: Power_Tuning_Map[n,m,p] $\leftarrow$ laser power
13: WL_Tuning_Map[n,m,p] $\leftarrow$ laser wavelength
14: **end for**
15: **end for**
16: **end for**
17: **Return** Power_Tuning_Map, WL_Tuning_Map, i_{R1}, i_{R2}, i_{PS}

the largest element of the cross-correlation matrix are related to the incremental heater powers required in the two rings in order to track a target laser output power maximum. We apply cross-correlation to all sequential pairs of tuning maps to track the maximum across the range of PS powers. Once all the data are processed, we have a set of triplets (I_{R1}, I_{R2}, I_{PS}) that allows us to follow a specific longitudinal laser mode. Finally, we extract the relation among the currents using a linear fitting.

The use of the cross-correlation (line 13 of Algorithm 2) is central in the mode-hop-free algorithm, so we highlight a few important remarks: (i) Algorithm 2 works only if the tuning map is assembled by varying the currents quadratically (line 3–5 of Algorithm 1); indeed, each element of the cross-correlation matrix is the overlap between two matrices that have been *linearly shifted* one with respect to the other [55]; from (1), we also know that the spectrum *shifts linearly* with I^2; from these two considerations, the currents must change quadratically in order to preserve all the linear relations; (ii) before computing the cross-correlation, we normalized the tuning maps by removing the average value of the output power (line 4 and line 11). This is because we are interested only in the pattern variation between two sequential pairs of tuning maps, so we remove the useless background information; (iii) the cross-correlation between two $N \times M$ matrices is a matrix with size $2N + 1 \times 2M + 1$. If the two input matrices are identical, the largest element of the cross-correlation matrix is in position $(N + 1, M + 1)$ (e.g., in the case of two identical tuning maps, the pattern is not shifted). Based on this consideration, the shift is computed with respect to the central element of the cross-correlation matrix (line 15 and 16 Algorithm 2); (iv) the use of the cross-correlation averages all possible variations in the measurements, making the calibration

Algorithm 2: Mode-Hop-Free Algorithm — Calibration.

Require: Power_Tuning_Map, i_{R1}, i_{R2}, i_{PS}
1: $N \leftarrow$ length of i_{R1}
2: $M \leftarrow$ length of i_{R2}
3: $P \leftarrow$ length of i_{PS}
4: $m_A =$ mean(Power_Tuning_Map[:,:,1])
5: $A =$ Power_Tuning_Map[:,:,1] - m_A
6: $i, j \leftarrow$ Find the indices of a local maximum of A
7: $I_{R1}[1] = i_{R1}[i]$
8: $I_{R2}[1] = i_{R2}[j]$
9: $I_{PS}[1] = i_{PS}[1]$
10: **for** $p = 2 : P$ **do**
11: $m_B =$ mean(Power_Tuning_Map[:,:,p])
12: $B =$ Power_Tuning_Map[:,:,p] - m_B
13: X $\leftarrow$ Compute the cross-correlation between A and B
14: $\alpha, \beta \leftarrow$ Find the indices of the largest element in X
15: $\Delta i = \alpha - N$
16: $\Delta j = \beta - M$
17: $i = i + \Delta i$
18: $j = j + \Delta j$
19: $I_{R1}[p] = i_{R1}[i]$
20: $I_{R2}[p] = i_{R2}[j]$
21: $I_{PS}[p] = i_{PS}[p]$
22: $A = B$
23: **end for**
24: $m_1, I^2_{R1,0} \leftarrow$ Linear fit: $I^2_{R1} = m_1 I^2_{PS} + I^2_{R1,0}$
25: $m_2, I^2_{R2,0} \leftarrow$ Linear fit: $I^2_{R2} = m_2 I^2_{PS} + I^2_{R2,0}$
26: **Return** m_1, m_2, $I^2_{R1,0}$, $I^2_{R2,0}$

method more robust than simply tracking for a target maximum, improving upon the previously reported method [23].

For the linear fitting (line 24 and 25 of Algorithm 2), we set the current of the phase shifter, I_{PS}, as an independent variable, and the currents of the rings, I_{R1} and I_{R2}, as the dependent variables:

$$I^2_{R1} = m_1 I^2_{PS} + I^2_{R1,0} \tag{2a}$$

$$I^2_{R2} = m_2 I^2_{PS} + I^2_{R2,0} \tag{2b}$$

Using I_{PS} as the independent variable is an arbitrary choice, and equivalent results can be obtained by replacing it with I_{R1} or I_{R2}. In (2), $I_{R1,0}$ and $I_{R2,0}$ are the currents in the ring heaters that provide a local maximum of the laser output power when the PS heater is off. The results of our fitting is a post-process analysis, and the linear coefficient m_1 and m_2 are extracted from Fig. 8.

The graph in Fig. 9 shows the laser wavelength and the output power when a specific peak is tracked as a function of the PS power. The wavelength changes linearly with the PS power while the output power is roughly constant.

The relationship between the current in the heaters is not the only aspect that contributes to mode-hop-free tuning, but the maximum tuning rate also has a substantial impact. If the heater powers are adjusted too quickly, it can result in mode hops in the laser behavior. To determine the maximum scanning speed

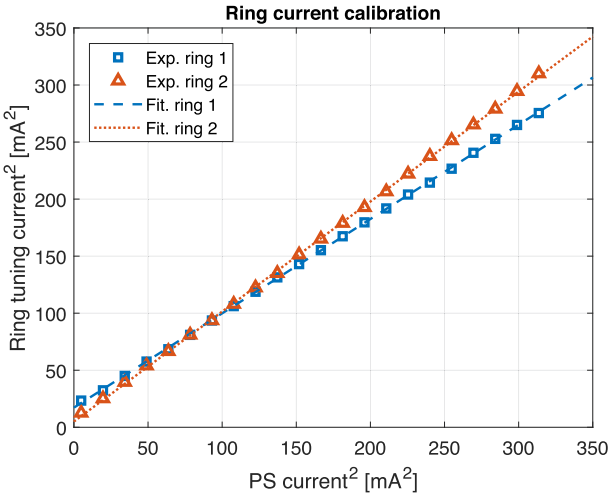

Fig. 8. Squared currents in the two rings as a function of the squared current in the phase shifter. The measured result show a linear relationship. Least-squares fit is used to estimate the coefficients in (2), producing $m_1 = 0.827$ and $I_{R1,0} = 4.149$ mA for the bottom ring in Fig. 1(b), and $m_2 = 0.964$ and $I_{R2,0} = 2.238$ mA for the top ring in the same figure. The mean error of the fitting on the input data is 1.066 mA^2 and 1.269 mA^2 for the two rings.

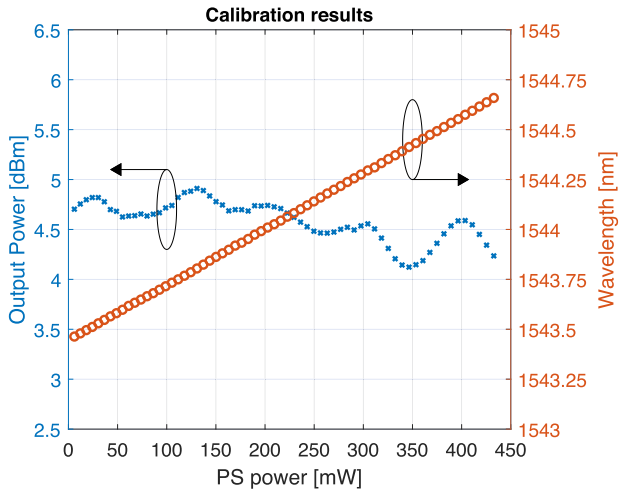

Fig. 9. Calibration results of the mode-hop-free tuning algorithm. Tracking a local peak of the output power as a function of the heating power of the two rings and the phase shifter.

of this laser we recall the theory of dynamic systems [56], [57]. The temperature variation in the heaters can be modeled as a first-order, linear, time-invariant, lumped element [42]. If the response time of the heaters is τ, its normalized impulse response is

$$h(t) = (-p)\, e^{pt}\, \delta_{-1}(t) \tag{3}$$

where t is the time variable, $p = -1/\tau$ is the pole of the system, and $\delta_{-1}(t)$ is the Heaviside step function. To tune the laser wavelength, we can linearly change the temperature of the cavity. Therefore, the input signal is proportional to a ramp function

$$u(t) = \left[\frac{t}{T}\,\delta_{-1} - \frac{t-T}{T}\,\delta_{-1}(t-T)\right] \tag{4}$$

where $u(t)$ varies between 0 and 1 in the time interval T. At this point, it is quite straightforward to calculate the change in laser wavelength over time as the convolution integral of the input signal and the impulse response of the system

$$\begin{aligned}\Delta\lambda(t) &= \Delta\lambda_M \int h(y)\, u(t-y)\, dy \\ &= \Delta\lambda_M \left[\frac{pt+1-e^{pt}}{pT}\delta_{-1}(t) \right. \\ &\quad \left. - \frac{p(t-T)+1-e^{p(t-T)}}{pT}\delta_{-1}(t-T) \right] \end{aligned} \tag{5}$$

Since $h(t)$ and $u(t)$ are normalized functions, the convolution integral is multiplied by $\Delta\lambda_M$, which is the maximum wavelength shift.

Eq. (5) is fundamental in determining the maximum tuning rate. Indeed, due to the non-zero response time of the heater, there will be a discrepancy between the target wavelength and the value of $\Delta\lambda$ at a specific time. During the scanning interval, for $0 < t < T$, the maximum error is

$$\begin{aligned} e_\lambda(t) &= \Delta\lambda_M \left| \frac{pt+1-e^{pt}}{pT} - \frac{t}{T} \right| \\ &= \Delta\lambda_M \left| \frac{1-e^{pt}}{pT} \right| \leq \left| \frac{\Delta\lambda_M}{pT} \right| = \tau \frac{\Delta\lambda_M}{T} \end{aligned} \tag{6}$$

To ensure a fast scan without mode hops, the laser wavelength must remain within the smallest mode-hop-free range of the laser, shown in Fig. 4, during the interval T. Eq. (6) allows us to find the maximum tuning rate, $\Delta\lambda_M/T$, where τ depends the heater response time and the maximum tolerable error on the tuning is determined by the laser.

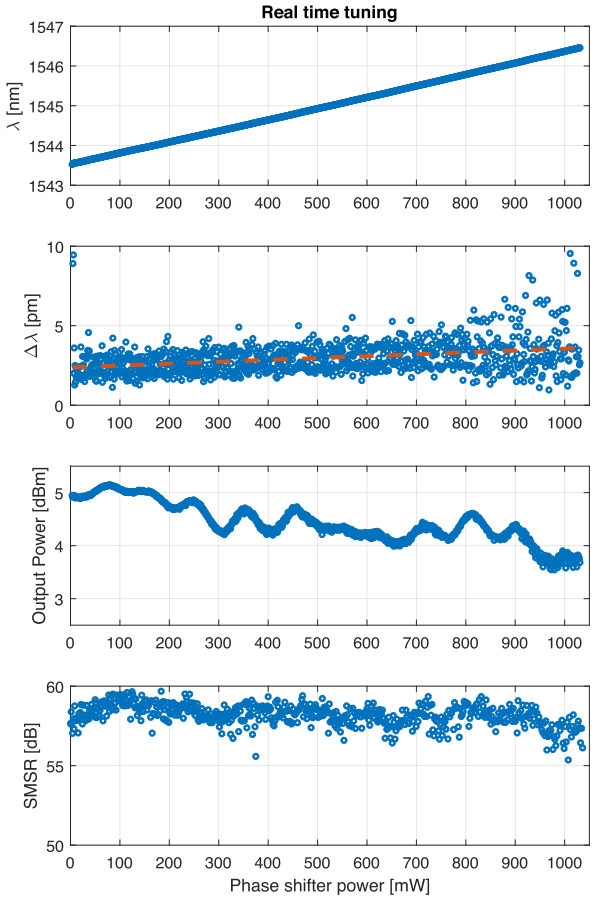

Fig. 10. Real time continuous tuning of the integrated laser. The results show mode-hop-free tuning over 3 nm, with an average incremental step $\Delta\lambda = 3 \pm 1$ pm, a variation of the output power of less than ± 1 dB, and a SMSR larger than 55 dB over the whole spectral range.

VI. Real-Time Mode-Hop-Free Tuning

To verify our algorithm, we sweep the currents in the three heaters using the coefficients we extracted previously. Fig. 10 collects the results of 1001 measurements, where the squared value of the currents in the PS, as well as the ones in the two ring heaters, are continuously increased in a coordinated manner. To keep track of any possible competing modes, lasing wavelengths are measured using a wavemeter with a spectral resolution of 0.1 pm (Yokogawa AQ6150). During the laser scan, we also measured the side-mode suppression ratio (SMSR) with an optical spectrum analyser.

The continuous tuning covers more than 3 nm and the fiber coupled power varies less than ± 1 dB. As shown in Fig. 10, each wavelength increment due to input current change is red-shifted by less than 10 pm, which is smaller than the mode hopping previously measured, $\simeq$60 pm. The large SMSR (>55 dB) and the small wavelength increment (<10 pm) confirm the single-mode operation and the continuous mode-hop-free tuning occur over the whole range.

The continuous tuning efficiency with respect to the phase shifter is 3 ± 1 pm/mW, which is the minimum step size in the current measurement system. In the current set-up, the accuracy of the steps is limited by the precision of the source measure units that control the current of the heaters (Keithley 2602 A). From the same measurements, we also extracted the efficiency of the ring heaters, which are 68 ± 2 mW/FSR and 79 ± 3 mW/FSR for the ring with radius 62.5 μm and 60 μm, respectively, and the efficiency of the phase shifter is 42 ± 1 mW/FSR. The lower efficiency of one of the two heaters (i.e., 79 mW/FSR) is explained by its relative closer position to the electrical pads, while the phase shifter heater has a higher efficiency due to better thermal insulation (see mask layout in Fig. 1). Indeed, the larger metal contacts and pads surrounding the top ring effectively drain the heat from the silicon ring, resulting in a higher power consumption per free-spectral-range.

In Fig. 11 the output spectra of the laser measured with an optical spectrum analyser (Yokogawa AQ6370D). For this instrument, the spectral resolution is 20 pm and allows us to verify that the ring resonators of the Vernier mirror are aligned and there are no other competing Vernier ring modes.

The duration required to carry out the analysis shown in Fig. 10 is limited by the time needed to record all spectra and takes approximately six minutes. However, a faster tuning rate can be performed. In this heterogeneous silicon photonics platform, the response time of the heaters, τ, is equal to

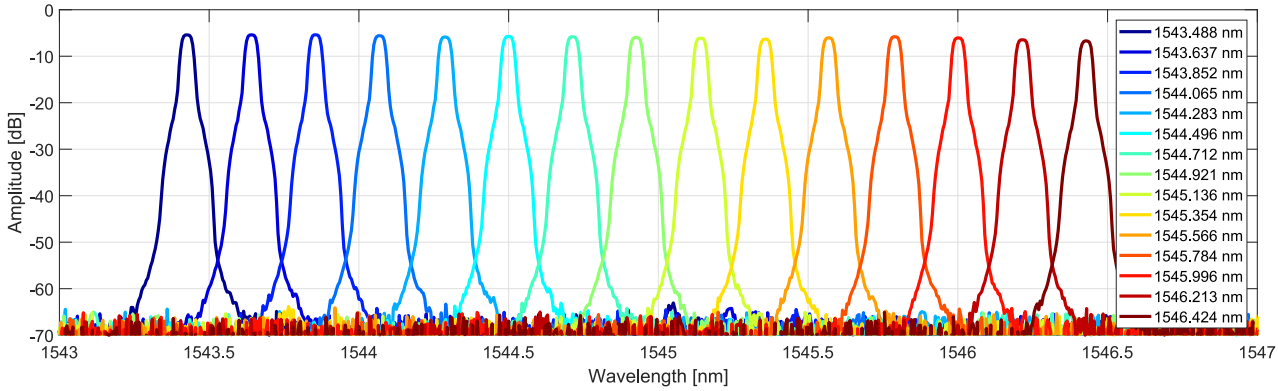

Fig. 11. Optical spectra of the integrated laser.

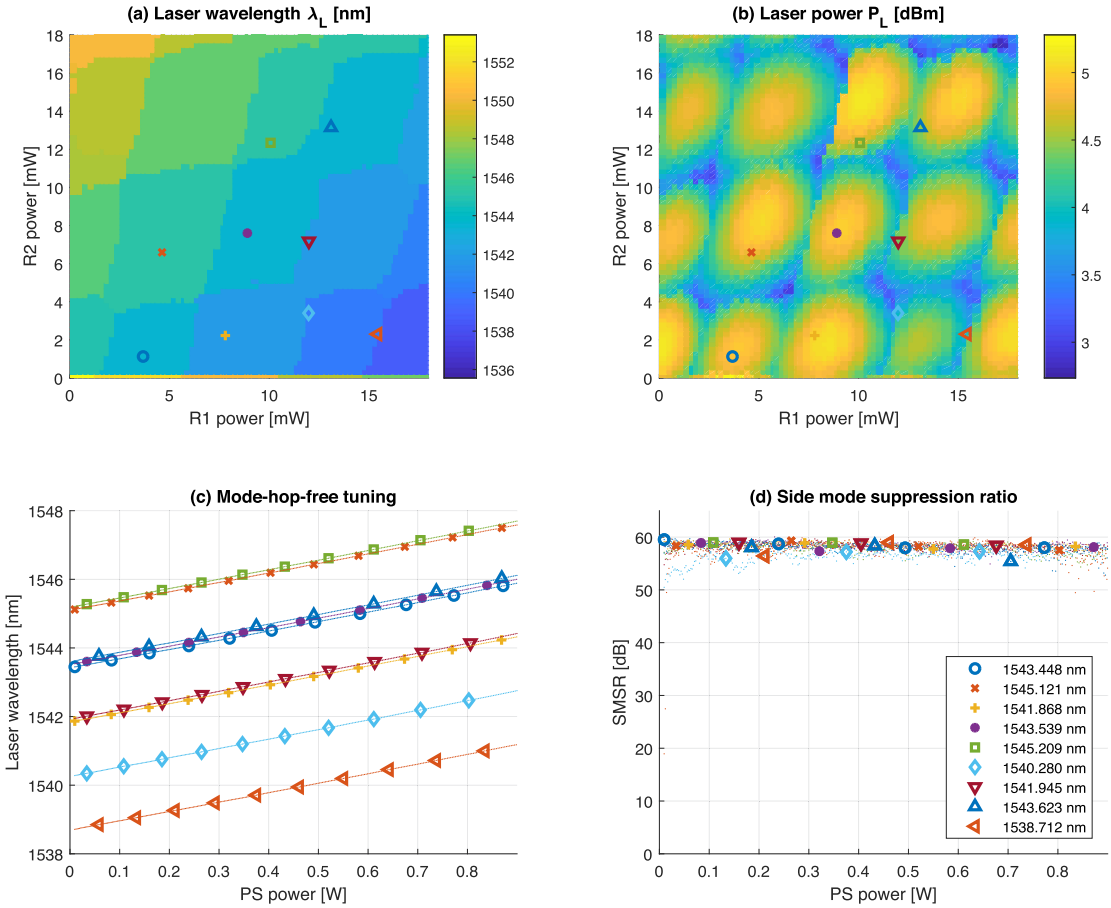

Fig. 12. Piece-wise mode-hop-free tuning. (a) 2D tuning map of the laser wavelength, λ_L, when the power of the phase shifter is 0 mW, (b) 2D tuning map of output power, P_L, when the power of the phase shifter is 0 mW, (c) Mode-hop-free laser tuning for different bias point, (d) SMSR for different operating conditions.

10 μs [58]. To estimate the maximum tuning rate that preserve the mode-hop-free scanning, we assume the largest tolerable error during the wavelength sweep must be smaller than 1 pm. This number is obtained from Fig. 4 by determining the maximum wavelength detuning in relation to the peak power before a mode-hop is observed. From (6), the tuning interval T can be as short as 30 ms, leading to a maximum tuning rate of 100 pm/ms (12.5 GHz/ms).

A tuning range larger than 10 nm can be reached by improving the design of the integrated heaters. In the current device, the 3 nm range is limited by the maximum heater power on the phase shifter, which is about 1.04 W, while the maximum power of the two ring heaters is 115 mW and 140 mW. Reducing the thickness of the top silica cladding layer from 1 μm down to 600 nm (i.e., the distance between metal heater and silicon layer) and optimizing the electrical pad location will reduce the

tuning power below 30 mW/FSR [42]. In addition, the heater efficiency can be doubled by creating lateral air trenches near the heaters [43], with a tuning power closer to 10 mW/FSR. The implementation of these two optimizations, will lead to a four-fold expansion in the continuous tuning range.

In the current design (and with the suggested improvements), we estimated a tuning rate larger than 10 GHz/ms. We would like to mention that the removal of the silicon substrate enables a much higher heater efficiencies and a larger tuning ranges [59], [60], [61]. However, this solution will increase the response time of the heaters by more than 10 times, resulting in slower laser tuning. To achieve a significantly faster tuning rate, the thermo-optic effect needs to be replaced with a faster tuning method, such as the electro-optic effects [24], [35], [36]. Despite this, the algorithm we proposed remains valid and can be utilized to calibrate the electro-optic tuning elements in order to determine the largest mode-hop-free tuning range.

VII. Piecewise Mode-Hop-Free Tuning

For some applications, it can be useful to cover a larger range of the optical spectrum than the one we demonstrated in the previous section. An effective solution is combining multiple segments of the spectrum to form a piecewise mode-hop-free sweep. Changing the bias point ($I^2_{R1,0}, I^2_{R2,0}$), the laser operates at a different Vernier resonance resulting in a different starting wavelength for the laser scan. Each lasing mode can be tuned continuously by coordinating the phase shifter with the heaters of the rings, as demonstrated previously. Fig. 12(a) and (b) show the tuning maps for the laser wavelength and the corresponding output power, respectively, when the electrical input power on the PS is 0 mW. The markers in the maps identify different bias points. Fig. 12(c) shows continuous laser tuning when the currents in the Vernier mirror are set to the different starting bias points, and then tuned using the algorithm. We also measured the SMSR of the laser, which is larger than 50 dB within all the intervals, as shown in Fig. 12(d). Stitching 1.5 nm wide mode-hop-free segments, we can span 6 nm of the optical spectrum in a piecewise continuous manner.

It has been previously demonstrated that the wavelength range of such a laser can span over 50 nm [19]. It is foreseeable that upon implementing the heater optimization described before, future integrated lasers can cover a similar range of spectrum with just 5 piece-wise mode-hop-free intervals.

VIII. Conclusion

In this work, we demonstrate an integrated narrow-linewidth laser in heterogeneous silicon photonics and we develop a robust method to continuously tune its emission wavelength over 3 nm (375 GHz). To the best of our knowledge, this is the largest tuning range without mode hopping demonstrated in this class of integrated laser architectures, and it outperforms the previous results by more than 13 times.

The large continuous tuning range is achieved by tracking the maximum of the laser output power. As such, the proposed solution can be easily implemented in portable systems, since it requires only an on-chip photodiode for laser power monitoring, a memory for data storage, and a digital signal processor for the calibration algorithm. This seamless integration with digital electronics together with the benefits offered by the laser hardware in terms of SWaP-C reduction, fast time response, and shock insensitivity, make the proposed approach ideal for portable optical coherent sensors like OFDR, OCT, and LiDAR systems.

The emission wavelength of the proposed laser is directly influenced by the resonant wavelength of the rings in the mirror. To achieve a wafer-scale Vernier laser with a wide mode-hop-free tuning range, post-fabrication trimming techniques can be employed to address fabrication variability [62], [63]. These techniques have proven to be highly effective in reducing variability among devices, minimizing the need for extensive algorithm adjustments across all devices.

In the current study, continuous tuning of the integrated laser was conducted in a nearly static state. Although the time response of each component may exhibit slight variations and the dynamic cross-talk may vary moderately compared to the static case, the value of 100 pm/ms (12.5 GHz/ms) provides a reliable estimate of the order of magnitude of the achievable tuning rate.

The tuning efficiency and tuning rate of the showcased laser can be further enhanced by optimizing the integrated tuning elements. Implementing lateral air trenches and a thinner silica cladding in the integrated heaters can enhance the tuning efficiency by four times, extending the mode-hop-free tuning range beyond 10 nm (1.25 THz). Achieving a faster tunability involves replacing the thermo-optic tunable elements with electro-optic ones. Tunable lasers on the $LiNbO_3$-on-insulator (LNOI) platform have been demonstrated to achieve frequency tuning rates that ranges from petahertz-per-second ($\sim$10 pm/μs) [35] up to exahertz-per-second ($\sim$10 pm/ns) [36], but their mode-hop-free tuning range is limited to only a few tens of gigahertz (a few hundreds of picometers). Utilizing $BaTiO_3$, which has recently been successfully demonstrated to be integrable on silicon photonics, can provide a much larger tuning range due to its 30 times higher electro-optic coefficient [64], [65], [66]. Although not yet demonstrated, fabricating tunable lasers with $BaTiO_3$-based electro-optic tunable elements can enable the same tuning rate as those in LNOI while achieving mode-hop-free tuning that spans hundreds of gigahertz (several namometers). Despite the hardware approach potentially being different, the same tuning algorithm presented in this article can still be applied.

Acknowledgment

The authors thank Mario Dumont, Theodore Morin, and Stephen Kreger for the helpful discussions. Any opinions, findings, and conclusions or recommendations expressed in this material are those of the authors and do not necessarily reflect the views of the NASA, U.S. Air Force, or DARPA.

References

[1] A. F. Fercher, "Optical coherence tomography," *J. Biomed. Opt.*, vol. 1, no. 2, pp. 157–173, 1996.

[2] A. F. Fercher, W. Drexler, C. K. Hitzenberger, and T. Lasser, "Optical coherence tomography-principles and applications," *Rep. Prog. Phys.*, vol. 66, no. 2, pp. 239–303, 2003.

[3] W. Eickhoff and R. Ulrich, "Optical frequency domain reflectometry in single-mode fiber," *Appl. Phys. Lett.*, vol. 39, no. 9, pp. 693–695, 1981.

[4] B. J. Soller, D. K. Gifford, M. S. Wolfe, and M. E. Froggatt, "High resolution optical frequency domain reflectometry for characterization of components and assemblies," *Opt. Exp*, vol. 13, no. 2, pp. 666–674, 2005.

[5] E. Strzelecki, D. Cohen, and L. Coldren, "Investigation of tunable single frequency diode lasers for sensor applications," *J. Lightw. Technol.*, vol. 6, no. 10, pp. 1610–1618, Oct. 1988.

[6] B. Behroozpour, P. A. M. Sandborn, M. C. Wu, and B. E. Boser, "Lidar system architectures and circuits," *IEEE Commun. Mag.*, vol. 55, no. 10, pp. 135–142, Oct. 2017.

[7] W. Xie et al., "Heterogeneous silicon photonics sensing for autonomous cars," *Opt. Express*, vol. 27, no. 3, pp. 3642–3663, Feb. 2019.

[8] C. E. Wieman and L. Hollberg, "Using diode lasers for atomic physics," *Rev. Sci. Instrum.*, vol. 62, no. 1, pp. 1–20, 1991.

[9] D. K. Serkland et al., "VCSELs for atomic sensors," *Proc. SPIE*, vol. 6484, 2007, Art. no. 648406.

[10] S. T. Kreger et al., "Optical frequency domain reflectometry: Principles and applications in fiber optic sensing," *Proc. SPIE*, vol. 9852, 2016, Art. no. 98520T.

[11] O. J. Ohanian et al., "OFDR on photonic circuits: Fiber optic sensing infrastructure and applications," in *Proc. Conf. Opt. Fiber Sensors*, 2018, Paper wB1.

[12] P. F. McManamon, *LiDAR Technologies and Systems*. Bellingham, WA, USA: SPIE, 2021.

[13] C. T. Santis, S. T. Steger, Y. Vilenchik, A. Vasilyev, and A. Yariv, "High-coherence semiconductor lasers based on integral high-Q resonators in hybrid Si/III-V platforms," *Proc. Nat. Acad. Sci.*, vol. 111, no. 8, pp. 2879–2884, 2014.

[14] M. A. Tran, D. Huang, and J. E. Bowers, "Tutorial on narrow linewidth tunable semiconductor lasers using Si/III-V heterogeneous integration," *APL Photon.*, vol. 4, no. 11, 2019, Art. no. 111101.

[15] L. A. Coldren, G. A. Fish, Y. Akulova, J. Barton, L. Johansson, and C. Coldren, "Tunable semiconductor lasers: A tutorial," *J. Lightw. Technol.*, vol. 22, no. 1, pp. 193–202, Jan. 2004.

[16] R. Kazarinov and C. Henry, "The relation of line narrowing and chirp reduction resulting from the coupling of a semiconductor laser to passive resonator," *IEEE J. Quantum Electron.*, vol. 23, no. 9, pp. 1401–1409, Sep. 1987.

[17] B. Liu, A. Shakouri, and J. E. Bowers, "Wide tunable double ring resonator coupled lasers," *IEEE Photon. Technol. Lett.*, vol. 14, no. 5, pp. 600–602, May 2002.

[18] Y. Lin et al., "Characterization of hybrid InP-TriPleX photonic integrated tunable lasers based on silicon nitride (Si_3N_4/SiO_2) microring resonators for optical coherent system," *IEEE Photon. J.*, vol. 10, no. 3, Jun. 2018, Art. no. 1400108.

[19] M. A. Tran, D. Huang, J. Guo, T. Komljenovic, P. A. Morton, and J. E. Bowers, "Ring-resonator based widely-tunable narrow-linewidth Si/InP integrated lasers," *IEEE J. Sel. Topics Quantum Electron.*, vol. 26, no. 2, Mar./Apr. 2020, Art. no. 1500514.

[20] A. Malik, J. Guo, M. Tran, G. Kurczveil, D. Liang, and J. Bowers, "Widely tunable, heterogeneously integrated quantum dot O-band lasers on silicon," *Photon. Res.*, vol. 8, no. 10, pp. 1551–1557, 2020.

[21] Y. Fan et al., "Hybrid integrated InP-Si_3N_4 diode laser with a 40-Hz intrinsic linewidth," *Opt. Express*, vol. 28, no. 15, pp. 21713–21728, Jul. 2020.

[22] J. Guo, C. Xiang, T. J. Morin, J. D. Peters, L. Chang, and J. E. Bowers, "E-band widely tunable, narrow linewidth heterogeneous laser on silicon," *APL Photon.*, vol. 8, no. 4, 2023, Art. no. 046114.

[23] A. Van Rees et al., "Ring resonator enhanced mode-hop-free wavelength tuning of an integrated extended-cavity laser," *Opt. Express*, vol. 28, no. 4, pp. 5669–5683, 2020.

[24] S. Andreou, K. A. Williams, and E. A. J. M. Bente, "Electro-optic tuning of a monolithically integrated widely tuneable InP laser with free-running and stabilized operation," *J. Lightw. Technol.*, vol. 38, no. 7, pp. 1887–1894, Apr. 2020.

[25] B. Mason, G. Fish, S. DenBaars, and L. Coldren, "Widely tunable sampled grating DBR laser with integrated electroabsorption modulator," *IEEE Photon. Technol. Lett.*, vol. 11, no. 6, pp. 638–640, Jun. 1999.

[26] D. Derickson et al., "SGDBR single-chip wavelength tunable lasers for swept source OCT," *Proc. SPIE*, vol. 6847, 2008, Art. no. 68472P.

[27] D. Huang et al., "High-power sub-kHz linewidth lasers fully integrated on silicon," *Optica*, vol. 6, no. 6, pp. 745–752, Jun. 2019.

[28] R. Wang et al., "Widely tunable III–V/Silicon lasers for spectroscopy in the short-wave infrared," *IEEE J. Sel. Topics Quantum Electron.*, vol. 25, no. 6, Nov./Dec. 2019, Art. no. 1502412.

[29] Y. Zhao, Y. Li, and W. Huang, "Narrow-linewidth distributed feedback Moiré-grating laser for high-speed optical communications," *Appl. Opt.*, vol. 59, no. 12, pp. 3666–3672, Apr. 2020.

[30] K. Liu and M. G. Littman, "Novel geometry for single-mode scanning of tunable lasers," *Opt. Lett.*, vol. 6, no. 3, pp. 117–118, 1981.

[31] W. Trutna and L. F. Stokes, "Continuously tuned external cavity semiconductor laser," *J. Lightw. Technol.*, vol. 11, no. 8, pp. 1279–1286, Aug. 1993.

[32] J. Hult, I. S. Burns, and C. F. Kaminski, "Wide-bandwidth mode-hop-free tuning of extended-cavity GAN diode lasers," *Appl. Opt.*, vol. 44, no. 18, pp. 3675–3685, 2005.

[33] A. Liu and X. Zhang, "A review of MEMS external-cavity tunable lasers," *J. Micromechanics Microengineering*, vol. 17, no. 1, pp. R1–R13, 2006.

[34] K. Kasai, M. Nakazawa, Y. Tomomatsu, and T. Endo, "1.5 μm, mode-hop-free full c-band wavelength tunable laser diode with a linewidth of 8 kHz and a rin of -130 dB/Hz and its extension to the l-band," *Opt. Express*, vol. 25, no. 18, pp. 22113–22124, Sep. 2017.

[35] V. Snigirev et al., "Ultrafast tunable lasers using lithium niobate integrated photonics," *Nature*, vol. 615, no. 7952, pp. 411–417, 2023.

[36] M. Li et al., "Integrated pockels laser," *Nature Commun.*, vol. 13, 2022, Art. no. 5344.

[37] V. Jayaraman, Z.-M. Chuang, and L. A. Coldren, "Theory, design, and performance of extended tuning range semiconductor lasers with sampled gratings," *IEEE J. Quantum Electron.*, vol. 29, no. 6, pp. 1824–1834, Jun. 1993.

[38] S. Tabares, V. Polo, and J. Prat, "Fast wavelength thermal tuning of DFB lasers for ultra dense WDM-PONs," *IEEE Photon. Technol. Lett.*, vol. 34, no. 20, pp. 1085–1087, Oct. 2022.

[39] H. Ishii, F. Kano, Y. Tohmori, Y. Kondo, T. Tamamura, and Y. Yoshikuni, "Narrow spectral linewidth under wavelength tuning in thermally tunable super-structure-grating (SSG) DBR lasers," *IEEE J. Sel. Topics Quantum Electron.*, vol. 1, no. 2, pp. 401–407, Jun. 1995.

[40] Y. Matsui et al., "Narrow linewidth tunable semiconductor laser," in *Proc. IEEE Compound Semicond. Week [Includes 28th Int. Conf. Indium Phosphide Related Mater., 43rd Int. Symp. Compound Semicond.*, 2016, pp. 1–2.

[41] M. C. Larson, "Narrow linewidth tunable DBR lasers," in *Proc. IEEE Int. Semicond. Laser Conf.*, 2016, pp. 1–2.

[42] P. Pintus et al., "PWM-driven thermally tunable silicon microring resonators: Design, fabrication, and characterization," *Laser Photon. Rev.*, vol. 13, no. 9, 2019, Art. no. 1800275.

[43] P. Dong et al., "Low power and compact reconfigurable multiplexing devices based on silicon microring resonators," *Opt. Express*, vol. 18, no. 10, pp. 9852–9858, May 2010.

[44] M. A. Tran, "Heterogeneous silicon/III-V photonic integration for ultralow noise semiconductor lasers," Ph.D. dissertation, Univ. of California Santa Barbara, Santa Barbara, CA, USA, 2019.

[45] M. N. Sysak et al., "Hybrid silicon laser technology: A thermal perspective," *IEEE J. Sel. Topics Quantum Electron.*, vol. 17, no. 6, pp. 1490–1498, Nov./Dec. 2011.

[46] C. Zhang, D. Liang, G. Kurczveil, J. E. Bowers, and R. G. Beausoleil, "Thermal management of hybrid silicon ring lasers for high temperature operation," *IEEE J. Sel. Topics Quantum Electron.*, vol. 21, no. 6, pp. 385–391, Nov./Dec. 2015.

[47] M. L. Davenport, S. Skendžić, N. Volet, J. C. Hulme, M. J. Heck, and J. E. Bowers, "Heterogeneous silicon/III–V semiconductor optical amplifiers," *IEEE J. Sel. Topics Quantum Electron.*, vol. 22, no. 6, pp. 78–88, Nov./Dec. 2016.

[48] J. Richter, "Ultra-high-Q inverted silica microtoroid resonators monolithically integrated into a silicon photonics platform," Ph.D. dissertation, Rheinisch-Westfälische Technische Hochschule Aachen, Aachen, Germany, 2018.

[49] R. Marchetti, C. Lacava, L. Carroll, K. Gradkowski, and P. Minzioni, "Coupling strategies for silicon photonics integrated chips [invited]," *Photon. Res.*, vol. 7, no. 2, pp. 201–239, Feb. 2019.

[50] J. Galán, P. Sanchis, G. Sánchez, and J. Martí, "Polarization insensitive low-loss coupling technique between SOI waveguides and high mode field diameter single-mode fibers," *Opt. Express*, vol. 15, no. 11, pp. 7058–7065, 2007.

[51] R. Jones et al., "Heterogeneously integrated InP/silicon photonics: Fabricating fully functional transceivers," *IEEE Nanotechnol. Mag.*, vol. 13, no. 2, pp. 17–26, Apr. 2019.

[52] M. A. Tran, D. Huang, T. Komljenovic, J. Peters, A. Malik, and J. E. Bowers, "Ultra-low-loss silicon waveguides for heterogeneously integrated silicon/III-V photonics," *Appl. Sci.*, vol. 8, no. 7, 2018, Art. no. 1139.

[53] T. Kita, R. Tang, and H. Yamada, "Narrow spectral linewidth silicon photonic wavelength tunable laser diode for digital coherent communication system," *IEEE J. Sel. Topics Quantum Electron.*, vol. 22, no. 6, pp. 23–34, Nov./Dec. 2016.

[54] J. Heebner, R. Grover, and T. Ibrahim, *Optical Microresonator Theory*. Berlin, Germany: Springer, 2008.

[55] M. M. Petrou and C. Petrou, *Image Processing: The Fundamentals*. Hoboken, NJ, USA:Wiley, 2010.

[56] K. Ogata, *System Dynamics*. Englewood Cliffs, NJ, USA: Prentice-Hall, 1978.

[57] A. Giua and C. Seatzu, *Analisi Dei Sistemi Dinamici*. Berlin, Germany:Springer, 2009.

[58] M. A. Tran, C. Zhang, and J. E. Bowers, "A broadband optical switch based on adiabatic couplers," in *Proc. IEEE Photon. Conf.*, 2016, pp. 755–756.

[59] P. Dong et al., "Thermally tunable silicon racetrack resonators with ultralow tuning power," *Opt. Express*, vol. 18, no. 19, pp. 20298–20304, Sep. 2010.

[60] A. Masood et al., "Comparison of heater architectures for thermal control of silicon photonic circuits," in *Proc. IEEE 10th Int. Conf. Group IV Photon.*, 2013, pp. 83–84.

[61] N. J. D. Martinez et al., "Substrate removal for ultra efficient silicon heater-modulators," in *Proc. IEEE Opt. Interconnects Conf.*, 2017, pp. 15–16.

[62] M. M. Milosevic et al., "Ion implantation in silicon for trimming the operating wavelength of ring resonators," *IEEE J. Sel. Topics Quantum Electron.*, vol. 24, no. 4, Jul./Aug. 2018, Art. no. 8200107.

[63] H. Jayatilleka et al., "Post-fabrication trimming of silicon photonic ring resonators at wafer-scale," *J. Lightw. Technol.*, vol. 39, no. 15, pp. 5083–5088, Aug. 2021.

[64] S. Abel et al., "A hybrid barium titanate–silicon photonics platform for ultraefficient electro-optic tuning," *J. Lightw. Technol.*, vol. 34, no. 8, pp. 1688–1693, Apr. 2016.

[65] F. Eltes et al., "A $BaTiO_3$-based electro-optic pockels modulator monolithically integrated on an advanced silicon photonics platform," *J. Lightw. Technol.*, vol. 37, no. 5, pp. 1456–1462, Mar. 2019.

[66] S. Abel et al., "Large pockels effect in micro-and nanostructured barium titanate integrated on silicon," *Nature Mater.*, vol. 18, no. 1, pp. 42–47, 2019.